Probing the plasma chemistry in a microwave reactor used for diamond chemical vapor deposition by cavity ring down spectroscopy

Jie Ma,[1] James C. Richley,[1] Michael N. R. Ashfold,[1,a)] and Yuri A. Mankelevich[2]
[1]*School of Chemistry, University of Bristol, Bristol BS8 1TS, United Kingdom*
[2]*Skobel'tsyn Institute of Nuclear Physics, Moscow State University, Vorob'evygory, Moscow 119991, Russia*

(Received 31 July 2008; accepted 30 September 2008; published online 19 November 2008)

Absolute column densities of $C_2(a)$ and CH radicals and $H(n=2)$ atoms have been measured in a diamond growing microwave reactor operating with hydrocarbon/Ar/H_2 gas mixtures as functions of height (z) above the substrate surface and process conditions. The monitored species are each localized in the hot plasma region, where $T_{gas} \sim 3000$ K, and their respective column densities are each reproduced, quantitatively, by two-dimensional (r,z) modeling of the plasma chemistry. The $H(n=2)$ distribution is seen to peak nearer the substrate, reflecting its sensitivity both to thermal chemistry (which drives the formation of ground state H atoms) and the distributions of electron density (n_e) and temperature (T_e). All three column densities are found to be sensitively dependent on the C/H ratio in the process gas mixture but insensitive to the particular choice of hydrocarbon (CH_4 and C_2H_2). The excellent agreement between measured and predicted column densities for all three probed species, under all process conditions investigated, encourages confidence in the predicted number densities of other of the more abundant radical species adjacent to the growing diamond surface which, in turn, reinforces the view that CH_3 radicals are the dominant growth species in microwave activated hydrocarbon/Ar/H_2 gas mixtures used in the chemical vapor deposition of microcrystalline and single crystal diamond samples. © *2008 American Institute of Physics*. [DOI: 10.1063/1.3021095]

I. INTRODUCTION

The companion papers[1,2] have presented (i) a two-dimensional (2D) (r,z) model of the gas phase chemistry, composition, and transport within a microwave (MW) plasma enhanced chemical vapor deposition (MW-PECVD) reactor used for growing polycrystalline diamond films from activated $CH_4/Ar/H_2$ mixtures and (ii) spatially resolved line-of-sight infrared (quantum cascade laser) absorption measurements of CH_4 and C_2H_2 in such a reactor as a function of process conditions (e.g., source hydrocarbon, gas mixing ratios, total pressure, and input MW power). The present paper describes further complementary experimental investigations of the gas phase composition and the chemistry prevailing within this reactor, now focusing on selected radical species that are localized in the plasma region. Specifically, we report spatially resolved [i.e., as a function of height (z) above the substrate surface] measurements of C_2 radicals [in the first excited ($a\ ^3\Pi_u$) electronic state], CH radicals [in the ground ($X\ ^2\Pi$) state], and H atoms [in their first excited ($n=2$) state] obtained using the technique of cavity ring down spectroscopy (CRDS).[3] CRDS methods have been applied in previous studies of diamond growing environments—e.g., to detect CH_3 (Ref. 4) and CH (Ref. 5) radicals in hot filament (HF) activated CH_4/H_2 gas mixtures, NH radicals in HF activated $CH_4/NH_3/H_2$ gas mixtures,[6] $C_2(a)$ and CN radicals in an atmospheric pressure oxyacetylene flame[7,8] and $C_2(a)$ radicals in MW activated $CH_4/Ar/H_2$ mixtures.[9,10] We have also previously reported the application of CRDS methods to the studies of all three of the present target species [C_2 (in both its ground ($X\ ^1\Sigma_g^+$) state and the $a\ ^3\Pi_u$ state), CH(X), and $H(n=2)$] as part of a comprehensive combined experimental and modeling study of diamond chemical vapor deposition (CVD) using a dc arc jet operating with $CH_4/H_2/Ar$ gas mixtures.[11–15]

CRDS is an ultrasensitive multipass absorption technique, which yields the line-integrated absorbance (LIA) associated with the chosen probe transition with (for the present radical species) vibrational and rotational quantum state resolutions. Given adequate knowledge of the spectroscopy of the target species of interest, this LIA can be converted to an absolute column (i.e., along r) density in the quantum state probed by the transition. Converting this quantity to a *total* column density of the chosen species or to a local species number density can be a major challenge, however, given the very inhomogeneous distribution of gas temperatures ($T_{gas} \sim 3000$ K in the center of the plasma ball but only ~300 K at the inside edge of the CVD reactor) and species number densities along the probed column. As shown in our recent diagnosis of the gas phase environment in a dc arc jet reactor,[14,15] however, such data can be obtained by judicious intercomparison between experimental measurement and high level reactor modeling such as described in the preceding paper.[1]

Here we report spatially resolved absolute column density measurements of $C_2(a)$ and CH radicals in selected quantum states and of $H(n=2)$ atoms in MW activated $CH_4/Ar/H_2$ and $C_2H_2/Ar/H_2$ gas mixtures as functions of the CH_4 and Ar flow rates [$F(CH_4)$ and $F(Ar)$, respectively],

a)Author to whom correspondence should be addressed. Tel.: (117)-9288312/3. FAX: (117)-9250612. Electronic mail: mike.ashfold@bris.ac.uk.

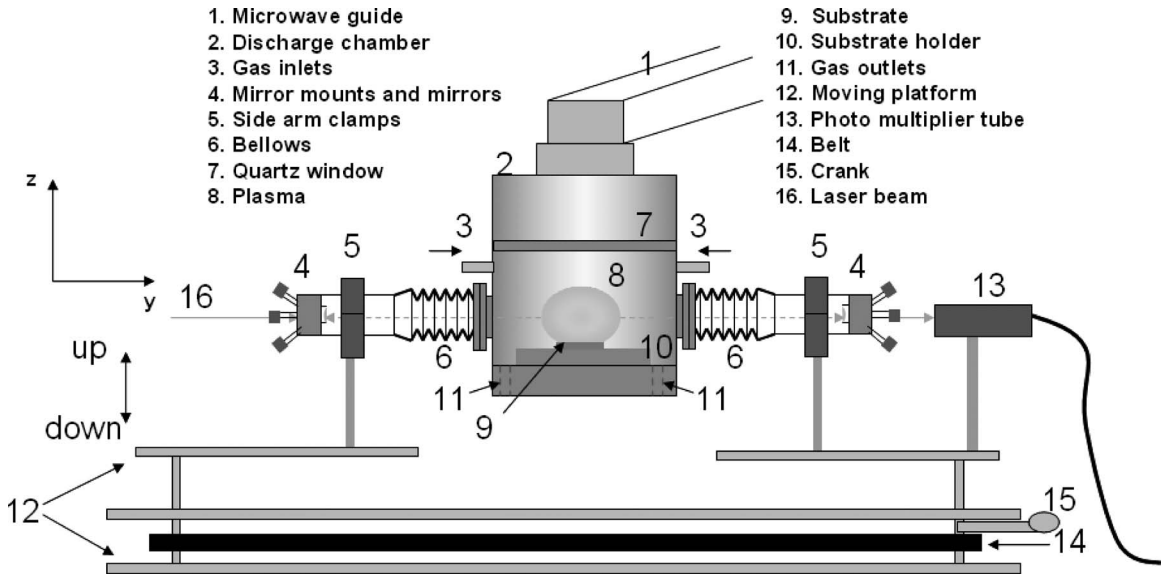

FIG. 1. Schematic diagram of the MW-PECVD reactor illustrating the position of the substrate, plasma ball, and the side arms for probing by CRDS.

the applied MW power P, and the total pressure p. The absolute column densities and the spatial profiles of all three monitored species are found to be sensitive to the carbon flow rate but insensitive to the choice of hydrocarbon. The companion 2D model calculations[1] reproduce the measured column densities essentially quantitatively, thereby affording new and detailed insights into the mechanisms by which gas is processed in and around the plasma ball and allowing reliable predictions of different reactive species number densities in the vicinity of the substrate on which diamond film growth occurs.

II. EXPERIMENTAL

The experimental setup is shown in Fig. 1. The hydrocarbon/Ar/H_2/plasma is excited by 2.45 GHz radiation in a purpose-designed and built MW-PECVD reactor (Element Six Ltd.), details of which have been presented previously.[2] For the present CRDS measurements, the diamond windows used for line-of-sight IR absorption measurements are replaced by tubular stainless steel side arms which are coupled to the reactor by flexible knife-edge bellow assemblies and terminate with finely adjustable mounts that hold high-reflectivity cavity end mirrors (LayerTec, Inc., $R>0.999$, planoconcave with 1 m radius of curvature). These side arms are mounted rigidly to a platform that supports all of the beam steering optics, and the complete optical assembly including the CRDS mirrors and the detector can be translated vertically with submillimeter precision, relative to the fixed MW reactor—thereby enabling spatially resolved line-of-sight column density measurements as a function of z, the vertical distance above the top surface of the 30 mm diameter Mo substrate. z values in the range of 0–25 mm are read from a rigidly mounted Vernier scale with $z=0$ established by finding the platform setting at which the substrate first impedes transmission of the probe laser beam (as revealed by a greatly perturbed ring down signal). The necessary tunable laser radiation was provided by a Nd doped yttrium aluminum garnet) pumped dye laser (Continuum Surelite III plus Spectra-Physics PDL-3) operating at a repetition rate of 10 Hz and wavelengths of ~515, ~431, and ~656.2 nm for CRDS detection of, respectively, $C_2(a,v=0)$ and $CH(X,v=0)$ radicals and $H(n=2)$ atoms. The dye laser bandwidth was ~0.1 cm^{-1}, and its wavenumber dispersion was monitored continuously during scanning by directing part of the beam into an etalon (free spectral range=0.85 cm^{-1}). The dye laser output was raised to the height of the center of the plasma ball using a periscope built from two 90° prisms (the upper of which was mounted on the translatable platform), passed through beam shaping optics (a spatial filter and a long focal length lens), and injected along the y axis. The transmitted light intensities were monitored behind the exit mirror using a photomultiplier tube. The ring down cavity (RDC) length $L=84$ cm, giving a near-confocal geometry and an estimated beam waist above the substrate of ~0.3 mm. All data collection and analysis used custom-written LABVIEW programs, communicating with an 8 bit digital oscilloscope (LeCroy 9361, dual channel, 300 MHz, 2.5 Gsamples/s) via a general purpose interface bus interface.

III. RESULTS

A. CRDS spectra and gas temperature determinations

Illustrative CRDS spectra of each of the three target species are displayed in Figs. 2(a)–2(c). Figure 2(a) shows a detailed view of a small portion of the $C_2(d\ ^3\Pi_g \leftarrow a\ ^3\Pi_u)$ (0,0) band. The three lines at lower wavenumber correspond to R branch transitions involving low J rotational levels, whereas the two features at higher wavenumber (the 19 246.9 cm^{-1} feature is actually a blend of two strong lines) are associated with transitions between high J levels in the P branch. The ratio of the low and high J line intensities is sensitive to the $C_2(a)$ rotational temperature—as illustrated in the lower part of Fig. 2(a), which shows simulations of this spectral region using PGOPHER,[16] appropriate

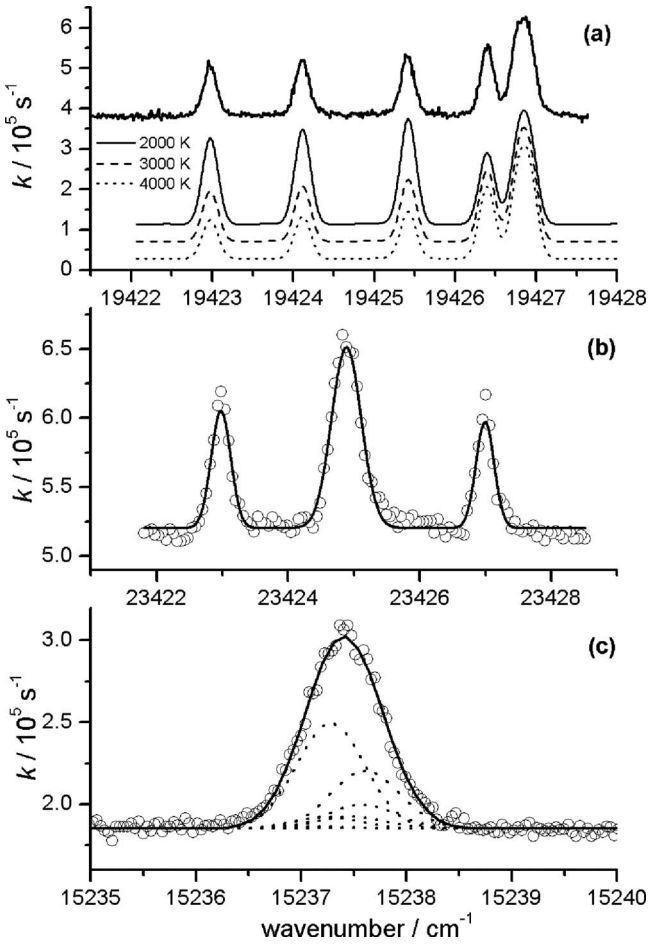

FIG. 2. Illustrative CRDS spectra of (a) part of the $C_2(d\ ^3\Pi_g \leftarrow a\ ^3\Pi_u)$ (0,0) band, (b) part of the CH($A\ ^2\Delta - X\ ^2\Pi$) (0,0) band, and (c) the H Balmer-α transition. The lower part of (a) shows simulations of this spectral region using PGOPHER, appropriate spectroscopic constants for the a and d states of C_2, a transition linewidth of 0.23 cm^{-1} (FWHM, Gaussian), and assumed temperatures T_{rot}=2000, 3000, and 4000 K—each offset vertically from one another and scaled such that the 19 426.88 cm^{-1} feature has the same peak intensity. The smooth curve in (b) is a best fit to the measured peaks assuming Gaussian lineshapes—for LIA determination. The smooth solid curve in (c) is a fit to the data points obtained by convoluting the seven fine-structure transitions shown by the dashed lines, all of which are assumed to have a common Gaussian lineshape and a (fitted) FWHM of 0.75 cm^{-1}.

spectroscopic constants for the a and d states of C_2 (Ref. 17) and assumed temperatures T_{rot}=2000, 3000, and 4000 K, respectively. Since collisions between the heavy species are very frequent at the high pressures ($75 \leqslant p \leqslant 175$ Torr) used in these experiments, rotational-translational (R-T) energy transfer processes are sufficiently efficient that these degrees of freedom are expected to be in local thermodynamic equilibrium throughout most of the reactor. Thus it is reasonable to equate T_{rot} with the gas temperature, T_{gas}. The gas temperature estimated by this method is $T_{gas} \sim 3000$ K [Fig. 2(a)] under all conditions used in the present experiments, confirming that the C_2 radical density is localized in the hot plasma ball.

As before,[14] given T_{gas}, the measured changes in ring down rate versus wavenumber ($\bar{\nu}$, in cm^{-1}) associated with a given spectral line can be converted to the absolute column density in the v=0 level, $\{C_2(a,v=0)\}$, using

$$\{C_2(a,v=0)\} = \frac{8\pi L\bar{\nu}^2}{A_{00}p_{line}}\int_{line} \Delta k d\bar{\nu}, \quad (1)$$

where L is the length of the RDC (84 cm). Δk is the wavenumber-dependent change in the ring down decay rate coefficient as a result of C_2 absorption, which is integrated over the full width of the rotational line of interest. A_{00} is the Einstein A coefficient for the $C_2(d-a)$ (0,0) band [$A_{00}=(7.21\pm0.30)\times10^6$ s^{-1} (Ref. 11)] and p_{line} is a line dependent weighting factor calculated with the PGOPHER spectral simulation program.[16] This (T dependent) factor is the calculated ratio of the integrated intensity of the spectral line under study to the total (0,0) band intensity (i.e., the sum of the integrated intensities of every rotational feature within the band). The $C_2(a)$ state is split into three spin-orbit manifolds (F_i, i=1–3) and each rotational level is further split by Λ doubling with the result that $p_{line}(J)=p_J/6$, where p_J is the rotational partition function given by the population ratio $p_J=[C_2(a,v=0,J)]/[C_2(a,v=0)]$. We will later compare the experimentally measured column densities with the corresponding quantities determined from the 2D model calculations using the equation

$$\{C_2(a,v=0)\} = \sum_{i=1}^{n} \Delta r_i [C_2(a)]_i p_{v=0}(T_i). \quad (2)$$

The index i in Eq. (2) labels each of the n cells of length Δr_i along the laser probe axis (i.e., along r). $[C_2(a)]_i$ and T_i are, respectively, the calculated $C_2(a)$ radical density and the temperature in the ith cell and $p_{v=0}(T_i)$ is the vibrational partition function. Equivalent formulas apply when analyzing measurements involving lines within the CH($A\ ^2\Delta - X\ ^2\Pi$) (0,0) band [Fig. 2(b)] with spectroscopic parameters taken from the study of Zachwieja[18] and $A_{00}=(1.85\pm0.05)\times10^6$ s^{-1} (Ref. 11). Features attributable to the CH($A-X$) (1,1) band are also observed weakly in the same wavelength range. Their intensities [relative to the (0,0) features] are sensibly consistent with the documented Franck–Condon factors and $T_{gas} \sim 3000$ K.

H(n=2) data were obtained by CRDS on the $n=3 \leftarrow n=2$ Balmer-α transition [Fig. 2(c)]. This transition was chosen in preference to Balmer-β ($n=4 \leftarrow n=2$) on account of its fivefold greater absorption cross section. In this case, it is not necessary to know T_{gas} in order to convert measured ring down data into column densities, but Einstein A coefficients are required for all fine-structure components of the transition.[19] As in the previous studies of H(n=2) atoms in a dc ac jet,[13,14,20,21] we assume that all spin-orbit components arising from the $2s^1$ and $2p^1$ electronic configurations are populated statistically according to their orbital degeneracies. Each of the resulting seven fine-structure transitions is given the same full width at half maximum (FWHM) linewidth, as illustrated in Fig. 2(c), and the convoluted lineshape that results compared with experiment. Such analysis establishes that the experimental line profile is described well assuming Gaussian lineshape functions—consistent with expectations that Doppler broadening will be the dominant contributor to the measured linewidth. (Stark broadening at the calculated[1] electron density $n_e \sim 3\times10^{11}$ cm^{-3} in the plasma ball center

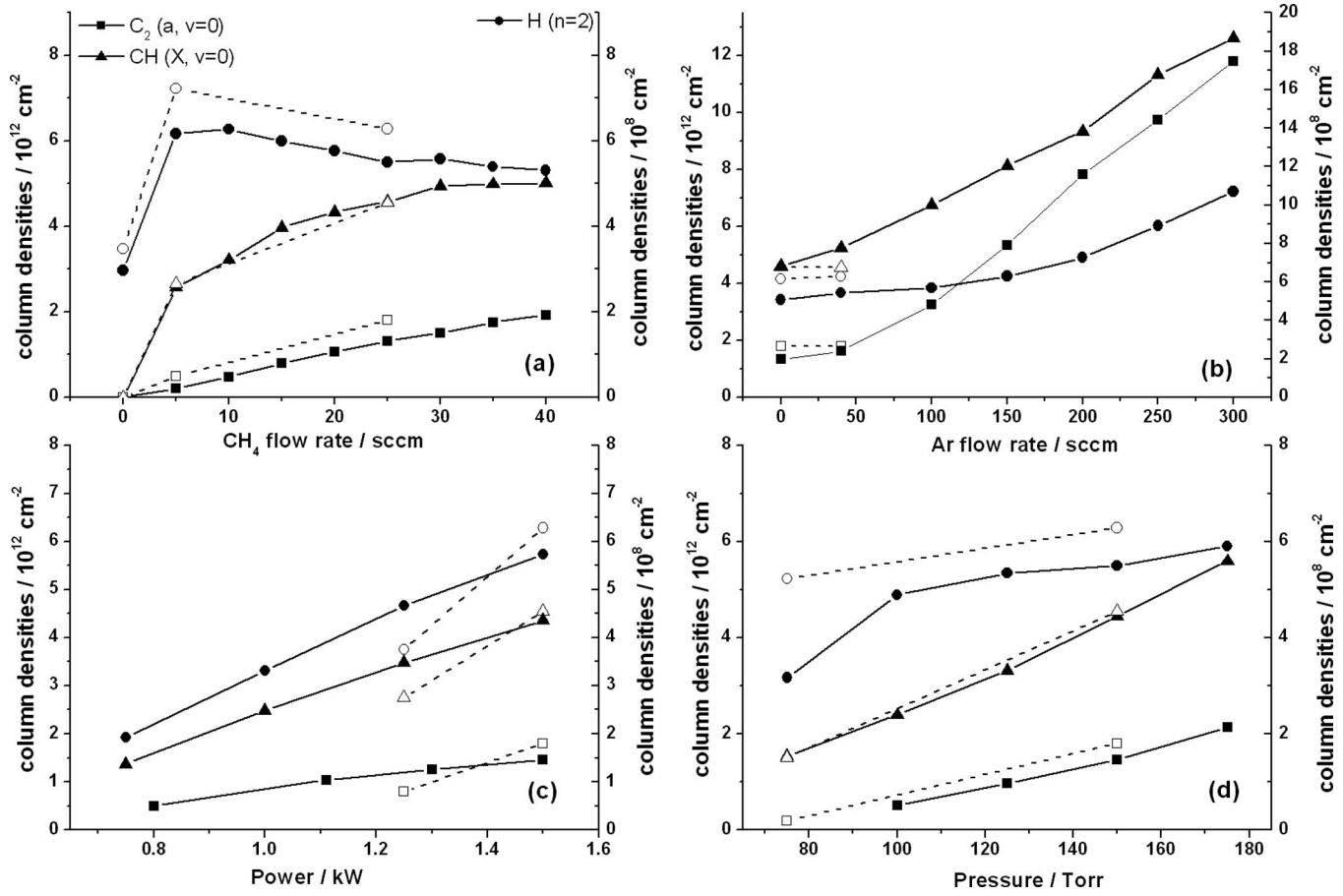

FIG. 3. Filled symbols: column densities for $C_2(a,v=0)$ and $CH(X,v=0)$ radicals (left hand scale) and for $H(n=2)$ atoms (right hand scale) measured at $z=11$ mm plotted as functions of (a) $F(CH_4)$, (b) $F(Ar)$, (c) applied MW power P, and (d) total pressure p. When recording the data in (a) and (b) $F(H_2)$ was adjusted in a compensatory manner to ensure that $F_{total}=565$ SCCM. The open symbols show values for the corresponding quantities returned by the 2D model calculations.

is negligible in comparison). However, the linewidth of each fine-structure transition returned by least-squares fitting to the measured lineshape is $\sim 0.75\ cm^{-1}$ (FWHM), which would imply $T\sim 4750$ K and is fully $0.1\ cm^{-1}$ larger than expected on the basis of $T_{gas}\sim 3000$ K. This FWHM value was found to be insensitive to all process parameters (e.g., the presence or otherwise of hydrocarbon in the plasma, the choice of hydrocarbon or the hydrocarbon mole fraction, the total pressure, or the input MW power). Exhaustive tests were also performed to confirm the laser bandwidth and the frequency dispersion of the measured spectra, and that the Balmer-α lineshape was insensitive to the laser power. No comparable "overbroadening" was found in our previous measurements of H Balmer-α and -β lineshapes in the arc jet plasma.[20,21] Anomalous H Balmer line widths have been reported in one previous high resolution optical emission study of MW activated $CH_4/Ar/H_2$ gas mixtures, however.[22] A possible explanation for this observation was presented in Paper I.[1] Most of the input power to a MW plasma is channeled into H_2 vibrational and/or rotational excitation via collisions with electrons. As a result, the H_2 vibrational population distribution is not in local thermal equilibrium. A significant fraction of this excitation energy is dissipated into gas heating via vibrational→translational ($V\rightarrow T$) energy transfer collisions with H atoms. The H Balmer linewidths observed in the present work can be understood, qualitatively, if the rate of $V\rightarrow T$ transfer to H atoms under the prevailing experimental conditions is comparable to the $T\rightarrow T$ relaxation rate of "hot" $H(n=1)$ and $H(n=2)$ atoms via elastic collisions with H_2, H, and Ar.

B. Column density measurements as functions of process conditions

Figure 3 shows column densities for $C_2(a,v=0)$ and $CH(X,v=0)$ radicals and for $H(n=2)$ atoms measured along the column at $z=11$ mm above the substrate surface. In all cases, the two radical column densities can be plotted conveniently on a common scale, indicated on the left hand axis of each plot. The $H(n=2)$ column densities are typically four orders of magnitude smaller—as shown on the right hand vertical axis in each of the plots. As in the companion studies,[1,2] the "base" process conditions were total flow rate $F_{total}=565$ SCCM (SCCM denotes cubic centimeters per minute at STP), comprising $F(CH_4)=25$ SCCM, $F(Ar)=40$ SCCM, and $F(H_2)=500$ SCCM, total pressure $p=150$ Torr, and input MW power $P=1.5$ kW. Also shown in Fig. 3 (open symbols) are the values returned by the 2D modeling after summing to obtain the corresponding column

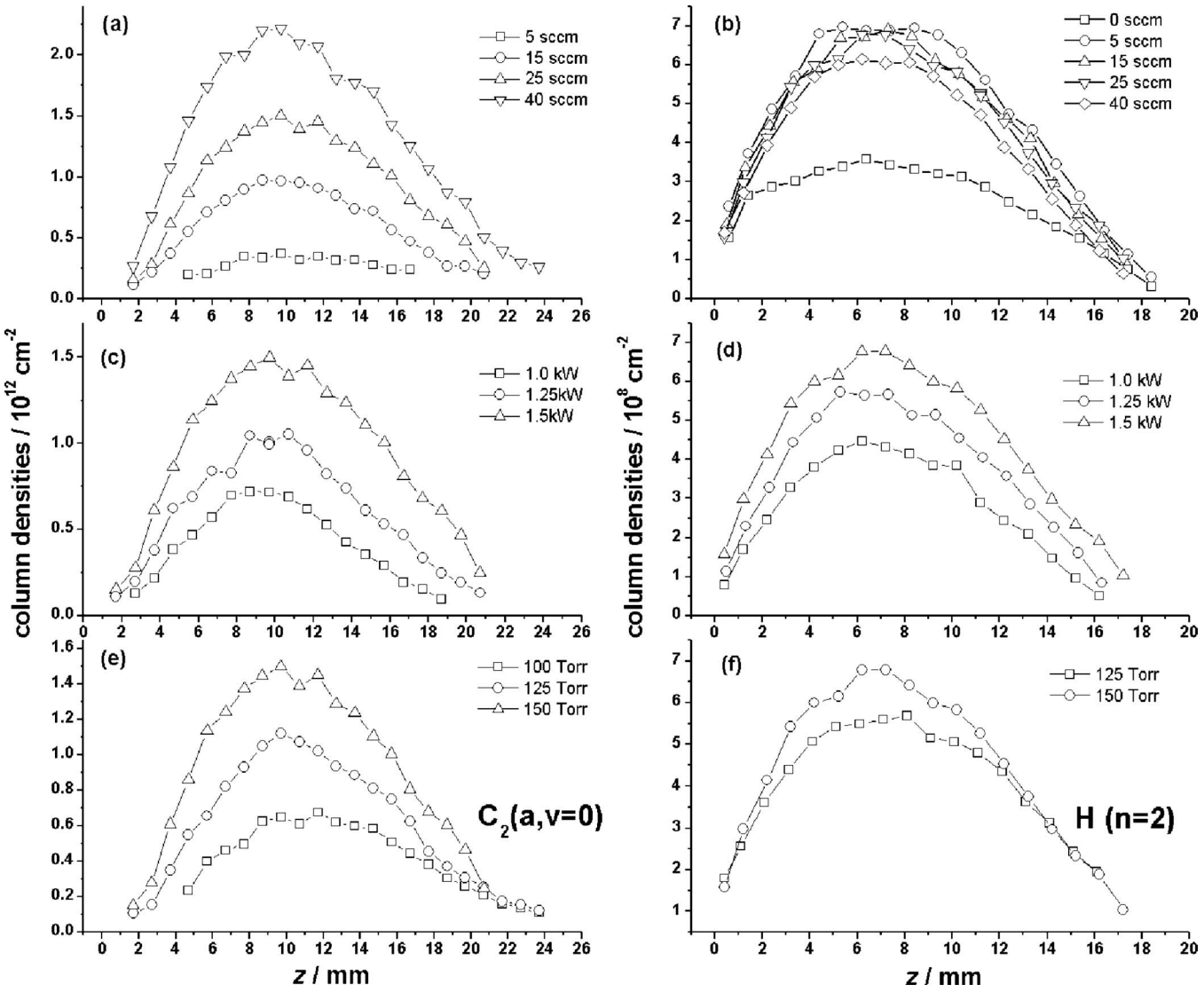

FIG. 4. Measured $C_2(a,v=0)$ radical and $H(n=2)$ atom column densities plotted as a function of probed height (z) above the substrate surface for different $F(CH_4)$ (top row), P (middle row), and p (bottom row). In each case, all parameters apart from the variable of interest were maintained at their base values—i.e., $F(Ar)=40$ SCCM, $F_{total}=565$ SCCM, $P=1.5$ kW, and $p=150$ Torr.

densities using Eq. (2). Clearly, the modeling succeeds in capturing both the absolute column densities and their variation with process conditions, well.

Each panel displayed in Fig. 3 illustrates the consequence of varying one parameter. Figure 3(a) shows the effect of varying $F(CH_4)$ from zero (a pure Ar/H_2 plasma) to 40 or 45 SCCM [with a compensatory adjustment of $F(H_2)$ to ensure that F_{total} remains constant]. Adding just 5 SCCM of CH_4 to the pure Ar/H_2 plasma results in an approximately twofold jump in the $H(n=2)$ column density, but further additions cause a progressive (small) decrease in this column density. The $C_2(a)$ column density is seen to scale essentially linearly with $F(CH_4)$, whereas the rate of increase in the $CH(X)$ column density declines with increasing $F(CH_4)$ to the extent that its value has reached a plateau by $F(CH_4)\sim 40$ SCCM. Figure 3(b) illustrates the changes in column density occurring as a result of varying $F(Ar)$ with, again, a compensatory change in $F(H_2)$ to ensure conservation of F_{total}. All three column densities increase as $F(Ar)$ is raised from 0 to 300 SCCM with that for $C_2(a)$ showing the steepest growth: the ratio of the $CH(X,v=0)$ to $C_2(a,v=0)$ column densities falls more than threefold across this range of $F(Ar)$. All three column densities increase (roughly in proportion) as P is increased from 0.75/0.8 to 1.5 kW [Fig. 3(c)]. As Fig. 3(d) shows, increasing p from 75 to 175 Torr also leads to an increase in all three column densities. The $CH(X,v=0)$ and $C_2(a,v=0)$ column densities generally retain their relative proportion, but the $H(n=2)$ column density clearly increases more slowly once $p>100$ Torr.

Figure 4 shows the way in which the $C_2(a)$ and $H(n=2)$ column densities vary as a function of probed height (z) above the substrate surface. The vertical profile of the $C_2(a)$ column densities changes minimally upon changing $F(CH_4)$, P, and p, peaking at $z\sim 10$ mm and with a FWHM of ~ 12 mm. The vertical profiles of the $CH(X)$ column densities were measured in equivalent detail and found to be very similar to those of $C_2(a)$ and similarly insensitive to this same set of process parameters. The right hand panel in Fig. 4 shows the corresponding vertical profiles of the

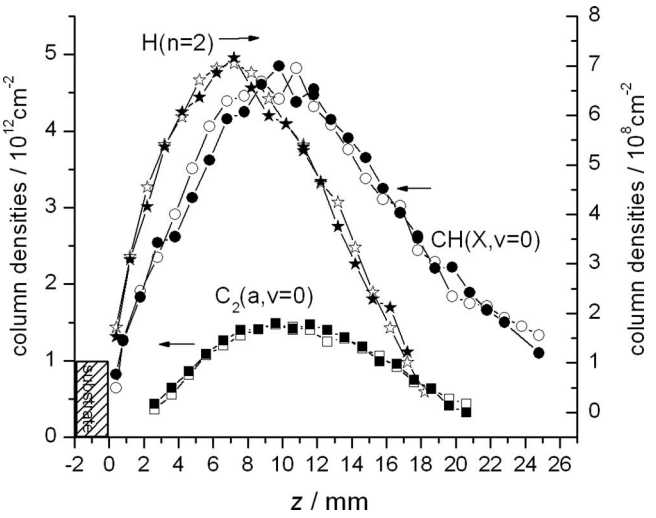

FIG. 5. Comparison of the spatially resolved column densities of $C_2(a,v=0)$ and $CH(X,v=0)$ radicals (left hand scale) and $H(n=2)$ atoms (right hand scale) measured when using (i) a $CH_4/Ar/H_2$ gas mixture at base conditions and (ii) a $C_2H_2/Ar/H_2$ gas mixture with $F(C_2H_2)=12.5$ SCCM and $F(H_2)$ increased to 512.5 SCCM (to ensure the same F_{total}) but otherwise identical process conditions.

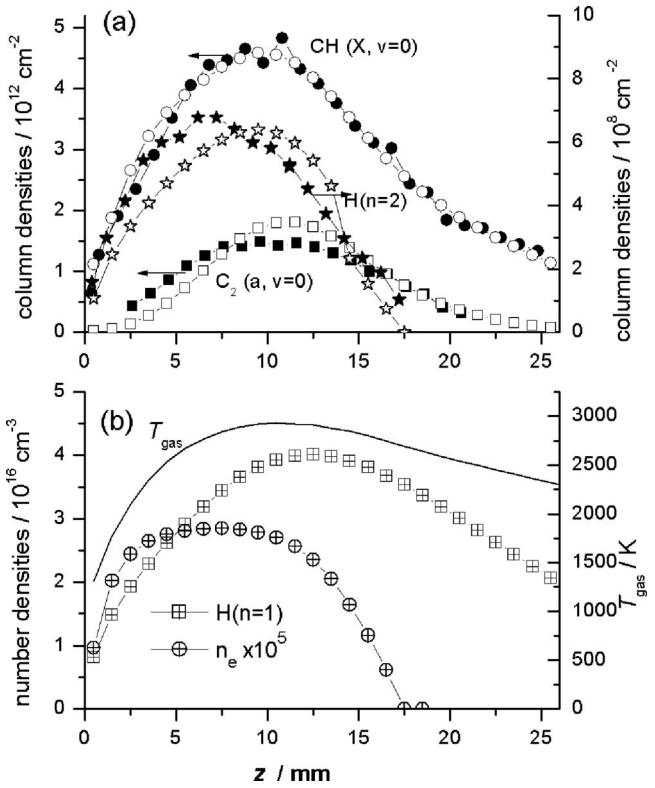

FIG. 6. (a) Comparison between the column density distributions of $C_2(a,v=0)$ and $CH(X,v=0)$ radicals (left hand scale) and $H(n=2)$ atoms (right hand scale) measured for a $CH_4/Ar/H_2$ gas mixture operating under base plasma conditions (filled symbols) and the corresponding quantities predicted by the 2D modeling and calculated using Eq. (2) (open symbols). (b) Plot showing the z dependence of n_e (at $r=0$) assumed in the 2D modeling, and the z dependences of the T_{gas} and $H(n=1)$ density distributions under base operating conditions that follow from this assumption.

$H(n=2)$ column densities. Several aspects of these data merit comment. First, all of the $H(n=2)$ profiles peak nearer the substrate ($z\sim 8$ mm) than the $C_2(a,v=0)$ and $CH(X,v=0)$ profiles. When $F(CH_4)>0$, the $H(n=2)$ profiles have a slightly smaller FWHM than those of $C_2(a,v=0)$ or $CH(X,v=0)$, but these broaden (and the column density shows an approximately twofold decrease) when $F(CH_4)$ is reduced to zero. The final point of note is the absence of profile data at the lower pressures. $H(n=2)$ column densities at $p=75$ Torr are plotted in Fig. 3(d), but the experiment is required to operate consistently for a much longer period (typically ~ 1 h) in order to measure a complete spatial profile such as any of those shown in Fig. 4. We were unable to maintain the necessary uniformity of performance over such time scales at low p due to the progressive growth of an (as yet unidentified) background absorption. This absorption could be flushed away by introducing a pulse of argon gas into the side arms to the reactor but persisted (almost indefinitely) if the plasma was extinguished and the gas flow and the pumping cut off. Studies at different wavelengths in the range of 430–660 nm indicate that the unknown absorption is broad and structureless, and that its buildup rate declines at longer wavelength and at higher pressure.

Figure 5 compares the spatial profiles of $C_2(a,v=0)$, $CH(X,v=0)$, and $H(n=2)$ species measured when using (i) a $CH_4/Ar/H_2$ gas mixture at base conditions and (ii) a $C_2H_2/Ar/H_2$ gas mixture with $F(C_2H_2)=12.5$ SCCM and $F(H_2)$ increased to 512.5 SCCM (to ensure the same carbon fraction and F_{total}) but otherwise identical process conditions. To within the measurement accuracy, the column density profile of each species is independent of the choice of hydrocarbon source gas. These data are arguably the most definitive yet reported to illustrate the point that the plasma chemistry and gas phase composition in the immediate vicinity of the growing diamond surface is insensitive to the particular carbon source—as required to explain the widespread applicability and success of the so-called Bachmann diagram.[23] This figure also serves to re-emphasize the offset of the $C_2(a,v=0)$ and $CH(X,v=0)$ profiles from that of the $H(n=2)$ atoms; the $H(n=2)$ profile peaks nearer the substrate (smaller z).

IV. DISCUSSION

A. Electronic versus thermal activation effects

The very different spatial profile of the $H(n=2)$ column density is understandable in the light of the mechanism by which $H(n=2)$ atoms are formed in the plasma region. $C_2(a)$ and $CH(X)$ radicals are both formed by thermal chemistry; their steady state concentrations and distributions are largely determined by the local T_{gas} and its effect on the position of the various equilibria within the C_1H_y and C_2H_x families of H-shifting reactions and on the rates of interconversion between these two sets of species. $H(n=2)$ atoms, in contrast, are energetic species ($E_{H(n=2)}\sim 10.2$ eV); population of this state under the prevailing plasma conditions is largely determined by electron impact excitation. The $H(n=2)$ column density distribution is thus determined by the convolution of the $H(n=1)$ population distribution—which is determined by thermal chemistry—and the distributions of electron density (n_e) and temperature (T_e). Figure 6(a) compares the experimentally measured $C_2(a,v=0)$, $CH(X,v=0)$, and $H(n=2)$

column density distributions for a $CH_4/Ar/H_2$ gas mixture and base plasma conditions with the corresponding quantities predicted by the 2D modeling and calculated using Eq. (2). These model outputs assume a "top-hat" T_e distribution [with an ~10% decrease adjacent to the substrate and a small (arbitrary) tail extending to larger z]. The calculated z dependence of the T_{gas}, H(n=1) and electron density distributions under base operating conditions (again at r=0) are also included in Fig. 6(b). It should be noted that the experimentally derived $C_2(a,v=0)$ and $CH(X,v=0)$ column densities shown here and in the preceding figures were derived from the measured LIAs using Eq. (1) and a constant p_{line} value appropriate for T_{gas}=3000 K, whereas the 2D model calculations show that T_{gas} is a function of z and r. In practice, however, the radical density is localized in a region where T_{gas} is fairly constant. The 2D model allows estimation of the possible error associated with the use of a fixed T_{gas} value; such analysis suggests that the experimentally derived profiles for both radical species overestimate the true profiles (by ~3% at the plasma center but by as much as 25% in the wings).

The model calculations clearly succeed in capturing the shift (to smaller z) in the maximum of the H(n=2) column density distribution relative to those of the two diatomic radical species. The small discrepancies between the observed and calculated maxima and the profiles of the H(n=2), $C_2(a,v=0)$, and $CH(X,v=0)$ species could certainly be reduced by optimizing the T_e distribution. For example, the T_e and n_e distributions predicted in the MW field and discharge simulations reported by Hassouni *et al.*[24] show maxima at small z and a more extensive tail extending to larger z—both of which modifications would have the effect of skewing the calculated H(n=2), $C_2(a,v=0)$, and $CH(X,v=0)$ distributions closer to that which is observed. Such refinements are outside the scope of present modeling, however, since the primary aims are prediction (and understanding) rather than fitting. However, the 2D model calculations show the values of the $C_2(a,v=0)$ and $CH(X,v=0)$ column densities to be quite sensitive functions of T_{gas} in the hot plasma region and thus allow rather precise prediction of the maximum gas temperature value (2920 ± 20 K).

Electronic effects also account for the observed approximately twofold jump in H(n=2) column density upon addition of $F(CH_4)$=5 SCCM to an Ar/H_2 plasma. The dominant ion in the pure Ar/H_2 plasma under our base conditions of F(Ar), F_{total}, p, and P is H_3^+ (with a number density $\sim 1.8\times10^{11}$ cm^{-3} near the plasma ball center). Addition of just 5 SCCM of CH_4 leads to a wholesale change in the ion chemistry and composition. The dominant ions are now $C_2H_3^+$ and $C_2H_2^+$ (with respective number densities in the center of the plasma ball of $\sim 2\times10^{11}$ and $\sim 5\times10^{10}$ cm^{-3}, cf. an H_3^+ number density of $\sim 1.2\times10^9$ cm^{-3}), a 35% increase in plasma density, and an increase in T_e from 1.26 to 1.324 eV. These increases in n_e and T_e account for the increase in H(n=2) column density. The model calculations also show that increasing $F(CH_4)$ further, from 5 to 25 SCCM, results in an increase in the $C_2H_2^+$ ion density (at the expense of $C_2H_3^+$), an ~10–20% increase in the overall ion (and electron) density and, importantly, a reduction in T_e (to ~1.277 eV). These latter variations tend to counterbalance one another and explain the experimental observation [Fig. 3(a)] that the H(n=2) column density is rather invariant to $F(CH_4)$ in the range $5 \leqslant F(CH_4) \leqslant 40$ SCCM.

Finally, of course, we note that electron impact excitation of H(n=1), Ar, C_2, CH, etc., species is responsible for the intense fluorescence from electronically excited species such as H($n>2$), $C_2(d)$, and $CH(A)$ that dominates the optical emission spectrum of the plasma in this and all similar MW reactors operating with C/H/(Ar) gas mixtures. The trends in optical emission intensities of each of these species as functions of process condition, their correlation with the column densities returned by CRDS, and thus their utility as a probe of the plasma chemistry and conditions are reserved for a future publication.[25]

B. Cycling of C_1H_y and C_2H_x species

Here we consider factors that determine $C_2(a,v=0)$ and $CH(X,v=0)$ column densities and their respective variations with process conditions. As shown previously,[1] it is instructive to consider the reactor volume in terms of three concentric shells, each supporting distinctively different chemical transformations. All three regions support H-shifting reactions within the respective C_1H_y and C_2H_x families, as well as $C_1H_y \leftrightarrow C_2H_x$ interconversion reactions—but with relative (and absolute) rates that are sensitively dependent on T_{gas}. The outermost coolest shell (C, $T_{gas}<1500$ K) is characterized by net $C_2H_x \rightarrow C_1H_y$ conversion. Under base conditions the 2D model calculations return $n_{CH_4} > n_{C_2H_2}$ throughout region C. Reducing $F(CH_4)$ to 5 SCCM reinforces this inequality, and the calculated n_{CH_4} in region C is $>10n_{C_2H_2}$. Such predictions are fully in accord with the results of our line-of-sight IR absorption measurements of CH_4 and C_2H_2 in this same reactor.[2]

Region B ($1500<T_{gas}<2500$ K), the annular shell around the central plasma region A), in contrast, is characterized by the net production of C_2H_x species, reflecting the effect of increased T_{gas} on the $C_1H_y \leftrightarrow C_2H_x$ interconversion rates. $n_{C_2H_2} > n_{CH_4}$ throughout region B and this inequality persists to smaller z (and r) to the extent that C_2H_2 accounts for >97% of all of the carbon in the plasma ball (region A, $T_{gas}>2500$ K) under our base conditions. Diffusive mixing between regions C (a source for C_1H_y species) and B (a source for C_2H_x species) is important in maintaining the balance between these two nonequilibrium regions. The extent of gas processing in regions B and C ensures that this result holds irrespective of the choice of input hydrocarbon. The rates of the $C_1H_y \leftrightarrow C_2H_x$ interconversion reactions are sufficiently high to ensure local equilibration and the C_1H_y/C_2H_x balance at any z within region B (and in region A) is simply determined by the local T_{gas} and H atoms mole fractions.

One, perhaps not widely recognized, characteristic of the plasma region (A) is the absence of significant sources or sinks of carbon containing gas phase species, except very near the substrate where, as Fig. 7 shows, the 2D modeling predicts two thin zones supporting significant (production-loss) rates. C_2H_x production is favored in the outer of these

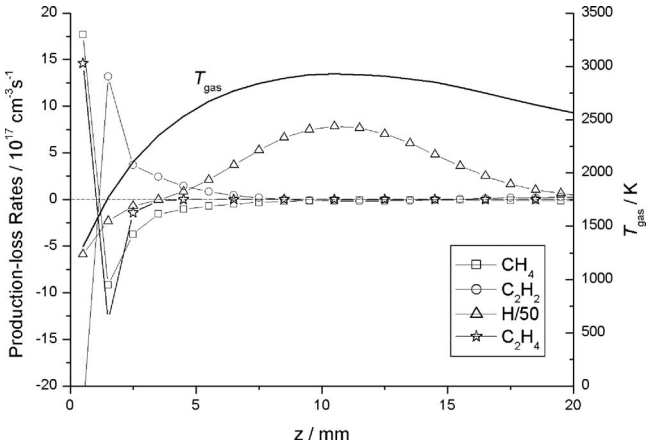

FIG. 7. Calculated (production-loss) rates of H atoms, CH_4, C_2H_2, and C_2H_4 (and T_{gas}) plotted as functions of z (at $r=0$) for standard process conditions: $F(CH_4)=25$ SCCM, $F(Ar)=40$ SCCM, $F(H_2)=500$ SCCM, $p=150$ Torr, $P=1.5$ kW, and $T_{sub}=973$ K.

two zones, centered at $z\sim 2$ mm, whereas $C_2H_x \rightarrow C_1H_y$ conversion is enhanced at yet smaller z. These zones are compressed analogs of regions B and C recognized at large z and are predicted to support similar net chemical transformations because of the similarities in T_{gas}. These concentration gradients and the steep gradient in T_{gas} caused by the proximate substrate will both encourage diffusion and thermal diffusion and species mixing in this near-substrate region of the plasma.

H-shifting rates in the bulk of region A are typically $\sim 10^{20}$ cm^{-3} s^{-1} for both the C_1H_y and C_2H_x families of species (i.e., $C_1H_y \leftrightarrow C_1H_{y-1}$ shifting reactions occur on a microsecond time scale). Rates linking the C_1H_y and C_2H_x families are slower ($\sim 10^{16}$ cm^{-3} s^{-1}) but still fast—corresponding to transformations on the time scale of tens of milliseconds under base conditions. Thus the $CH(X,v=0):C_2(a,v=0)$ ratio is simply determined by the equilibrium between the C_1H_y and C_2H_x families, and carbon conservation requires that $[C_1H_y] \propto [C_2H_x]^{0.5}$.[1] Given that almost all of the carbon in region A is in the form of C_2H_2, increasing the input carbon flow rate (from whatever hydrocarbon source) can be predicted to cause a linear increase in measured C_2 column density (given its proportionality to C_2H_2 through the H-shifting reactions) and a square root dependence on the C_1H_y densities—including the measured $CH(X,v=0)$ column density—as observed [Fig. 3(a)].

Increasing F(Ar) results in a decrease in the $CH(X,v=0):C_2(a,v=0)$ ratio [Fig. 3(b)]. Replacing H_2 by Ar reduces the thermal conductivity of the gas mixture with the result that T_{gas} (and thus the n_H/n_{H_2} ratio) is predicted to increase. A small increase in T_{gas} would not be discernible via the present $C_2(a)$ rotational temperature determinations but would suffice to increase the C_2H and C_2 densities since the thermal dissociation rates of C_2H_2 and C_2H are rather sensitive functions of T_{gas} at these high gas temperatures. Quite small increases in T_{gas} could thus account for the observed increase in $C_2(a,v=0):CH(X,v=0)$ ratio upon increasing F(Ar). Increasing total p also causes this ratio to increase [Fig. 3(d)]. This, too, can be traced to the small increase in T_{gas} that accompanies the modest decrease in plasma ball volume that results from an increase in p. Inspection of the plasma chemistry mechanism used in the 2D modeling highlights another possible source of C_2 (and C_2H) radicals—electron impact induced dissociation of C_2H_2 and C_2H. This is not an important source under the present plasma conditions but will become an increasingly important contributor to the total C_2 density in the plasma ball at higher argon dilutions (e.g., >90% Ar) and thus at the higher electron densities and temperatures realized in MW activated growth of ultrananocrystalline diamond.[26]

TABLE I. Predicted densities of the more abundant small carbon containing radical species close to the substrate under base conditions (4.4%CH_4/7%Ar/balance H_2, $p=150$ Torr, input power $P=1500$ W, absorbed power density $Q_J \sim 20-40$ W cm^{-3}, and $T_{sub}=973$ K).

z (mm)	0.5	1.5
T_{gas} (K)	1305	1772
Species	Species density/cm^{-3}	
CH_3	1.1×10^{14}	1.3×10^{14}
$^3CH_2$	4.6×10^{11}	2.5×10^{12}
$^1CH_2$	1.1×10^{10}	1.3×10^{11}
CH	1.7×10^{10}	1.8×10^{11}
C	5.1×10^{10}	6.5×10^{11}
C_2H_3	1.9×10^{13}	3.2×10^{12}
C_2H_2	1.1×10^{16}	6.4×10^{15}
C_2H	3.1×10^{10}	7.7×10^{11}
$C_2(X)$	1.5×10^{7}	7.3×10^{8}
$C_2(a)$	6.3×10^{7}	3.0×10^{9}
C_3	1.3×10^{13}	1.2×10^{13}
C_3H_2	2.1×10^{14}	1.1×10^{14}

C. C_1H_y and C_2H_x radical densities near the growing diamond surface

Experiment and 2D model predictions are in essentially quantitative agreement with regard to the column densities of $C_2(a)$ and $CH(X)$ radicals and $H(n=2)$ atoms in the present MW-PECVD reactor and to the value of T_{gas} in the plasma ball. Given this convergence and in the light of the perennial discussion regarding potential diamond growth species, it is instructive to consider the predicted densities of other C_1H_y and C_2H_x radical species near the growing diamond surface. Table I lists these values for base conditions, an absorbed power density, $Q_J=20$-40 W cm^{-3}, and $T_{sub}=973$ K. Several points merit note. CH_3 is the dominant carbon containing radical species at small z under the base conditions of the present study with C_2H_3 and C_3 the next most abundant at $z=0.5$ mm. If either of the latter actually accommodate on the diamond surface their subsequent fate is likely to involve hydrogenation and etching back into the gas phase via a β-scission mechanism.[27] T_{gas} falls rapidly on approaching the substrate, implying that the total number density increases as $z\rightarrow 0$. All of the C_1H_y radical densities are predicted to decrease over the range from $z=1.5$ to $z=0.5$ mm, however, most notably for the smaller ($y\leqslant 2$) species. This reflects the temperature dependences of the C_1H_y (and C_2H_x) H-shifting reactions, the equilibria for which favor $y=4$ and

$x=2$ at low T_{gas}, and is slightly exacerbated by C_1H_y gas-surface reactions on the growing diamond surface. Based on gas temperature considerations, we should anticipate further $C_1H_y \rightarrow CH_4$ and net $C_2H_2 \rightarrow CH_4$ conversion in the thin boundary layer adjacent to the diamond surface. The steep temperature gradients will encourage thermodiffusional mixing. The chemistry and composition in this $z<0.5$ mm region can thus be expected to be markedly nonequilibrium and to involve a mixture of hot (from the plasma region) and "cooler" (exsurface) species, the detailed treatment of which is beyond the scope of the present modeling. Nonetheless, the analysis reported here and in the accompanying papers[1,2] serves to reinforce the consensus view that CH_3 is the dominant radical species underpinning CVD in the process regime traditionally used for growth of microcrystalline and single crystal diamond.

V. CONCLUSIONS

Absolute column densities of $C_2(a)$, CH and $H(n=2)$ species have been measured in a MW-PECVD reactor operating with hydrocarbon/Ar/H_2 gas mixtures as a function of height (z) above the substrate surface and for a range of process conditions (choice of input hydrocarbon, hydrocarbon and argon mole fractions, pressure, and input power). The obtained column densities are in quantitative agreement with those predicted by companion 2D (r,z) modeling of the plasma chemistry prevailing in this reactor. All three of the monitored species are localized in the hot plasma region (A), where $T_{gas} \sim 2900$ K with the $H(n=2)$ distribution peaking at smaller z (~ 8 mm) than the distributions of $C_2(a)$ and CH radicals—reflecting the particular sensitivity of the former not only to the thermal chemistry [that drives $H(n=1)$ formation] but also to the distributions of electron density (n_e) and temperature (T_e). Measurements of $CH_4/Ar/H_2$ and $C_2H_2/Ar/H_2$ plasmas involving equivalent carbon flow rates yield indistinguishable column density distributions for all three probed species—thereby providing the most direct and definitive demonstration to date that the diamond CVD process itself is insensitive to the particular choice of carbon source gas. Under any given conditions of pressure and input power, the $C_2(a)$:CH ratio is shown to be a sensitive function of the C/H ratio in the feed gas, encouraging further consideration of the use of *in situ* measurements of this ratio as a means of process control. The quantitative agreement between measured and predicted column densities for all three probed species, under all process conditions investigated, encourages confidence in the predicted number densities of other of the more abundant radical species adjacent to the growing diamond surface. Consideration of the model outputs encourages the view that CH_3 radicals are the dominant growth species in MW activated hydrocarbon/Ar/H_2 gas mixtures currently used in the CVD of microcrystalline and single crystal diamond samples.

ACKNOWLEDGMENTS

The Bristol group is grateful to EPSRC for the award of a portfolio grant (LASER), to Element Six Ltd for financial support and the long term loan of the MW reactor, to the University of Bristol and the Overseas Research Scholarship (ORS) scheme for a postgraduate scholarship (J.M.), and to colleagues A. Cheesman, B. R. Coulson, J. J. Henney, and K. N. Rosser, to Dr. J. A. Smith and Dr. C.M. Western, and to Professor A. J. Orr-Ewing for their many contributions to the work described here. Y.A.M. is pleased to acknowledge support from RF Government for Key Science Schools under Grant No. 133.2008.2. The collaboration between Bristol and Moscow is supported by a Royal Society Joint Project Grant.

[1] Yu. A. Mankelevich, M. N. R. Ashfold, and J. Ma, "Plasma-chemical processes in microwave plasma enhanced chemical vapour deposition reactors operating with C/H/Ar gas mixtures," J. Appl. Phys. (accepted).
[2] J. Ma, A. Cheesman, M. N. R. Ashfold, K. G. Hay, S. Wright, N. Langford, G. Duxbury, and Yu. A. Mankelevich, "Quantum cascade laser investigations of CH_4 and C_2H_2 inter-conversion in hydrocarbon/H_2 gas mixtures during microwave plasma enhanced chemical vapor deposition of diamond," J. Appl. Phys. (submitted).
[3] M. D. Wheeler, S. M. Newman, A. J. Orr-Ewing, and M. N. R. Ashfold, J. Chem. Soc., Faraday Trans. **94**, 337 (1998).
[4] E. H. Wahl, T. G. Owano, C. H. Kruger, P. Zalicki, Y. Ma, and R. N. Zare, Diamond Relat. Mater. **5**, 373 (1996) and references therein.
[5] U. Lommatzsch, E. H. Wahl, T. G. Owano, C. H. Kruger, and R. N. Zare, Chem. Phys. Lett. **320**, 339 (2000).
[6] J. A. Smith, J. B. Wills, H. S. Moores, A. J. Orr-Ewing, M. N. R. Ashfold, Yu. A. Mankelevich, and N. V. Suetin, J. Appl. Phys. **92**, 672 (2002).
[7] A. Staicu, R. L. Stolk, and J. J. ter Meulen, J. Appl. Phys. **91**, 969 (2002).
[8] R. L. Stolk and J. J. ter Meulen, J. Chem. Phys. **117**, 8281 (2002).
[9] P. John, J. R. Rabeau, and J. I. B. Wilson, Diamond Relat. Mater. **11**, 608 (2002).
[10] J. R. Rabeau, P. John, J. I. B. Wilson, and Y. Fan, J. Appl. Phys. **96**, 6724 (2004).
[11] J. B. Wills, J. A. Smith, W. E. Boxford, J. M. F. Elks, M. N. R. Ashfold, and A. J. Orr-Ewing, J. Appl. Phys. **92**, 4213 (2002).
[12] C. J. Rennick, J. A. Smith, M. N. R. Ashfold, and A. J. Orr-Ewing, Chem. Phys. Lett. **383**, 518 (2004).
[13] C. J. Rennick, A. G. Smith, J. A. Smith, J. B. Wills, A. J. Orr-Ewing, M. N. R. Ashfold, Yu. A. Mankelevich, and N. V. Suetin, Diamond Relat. Mater. **13**, 561 (2004).
[14] C. J. Rennick, J. Ma, J. J. Henney, J. B. Wills, M. N. R. Ashfold, A. J. Orr-Ewing, and Yu. A. Mankelevich, J. Appl. Phys. **102**, 063309 (2007).
[15] Yu. A. Mankelevich, M. N. R. Ashfold, and A. J. Orr-Ewing, J. Appl. Phys. **102**, 063310 (2007).
[16] C. M. Western, PGOPHER, a program for simulating rotational structure, University of Bristol (http://pgopher.chm.bris.ac.uk).
[17] G. M. Lloyd and P. Ewart, J. Chem. Phys. **110**, 385 (1999).
[18] M. Zachwieja, J. Mol. Spectrosc. **170**, 285 (1995).
[19] http://physics.nist.gov/PhysRefData/ASD/index.html.
[20] C. J. Rennick, R. A. H. Engeln, J. A. Smith, A. J. Orr-Ewing, M. N. R. Ashfold, and Yu. A. Mankelevich, J. Appl. Phys. **97**, 113306 (2005).
[21] C. J. Rennick, J. Ma, M. N. R. Ashfold, A. J. Orr-Ewing, and Yu. A. Mankelevich, Plasma Sources Sci. Technol. **15**, 432 (2006).
[22] T. Lang, J. Stiegler, Y. von Kaenel, and E. Blank, Diamond Relat. Mater. **5**, 1171 (1996).
[23] P. K. Bachmann, D. Leers, and H. Lydtin, Diamond Relat. Mater. **1**, 1 (1991).
[24] K. Hassouni, T. A. Grotjohn, and A. Gicquel, J. Appl. Phys. **86**, 134 (1999).
[25] J. Ma, M. N. R. Ashfold, and Yu. A. Mankelevich, "Validating optical emission spectrscopy as a diagnostic of microwave activated $CH_4/Ar/H_2$ plasmas used for diamond chemical vapor deposition," J. Appl. Phys. (submitted).
[26] P. W. May and Yu. A. Mankelevich, J. Phys. Chem. C **112**, 12432 (2008).
[27] D. G. Goodwin and J. E. Butler, in *Handbook of Industrial Diamonds and Diamond Films*, edited by M. A. Prelas, G. Popovici, and L. K. Bigelow (Dekker, New York, 1998), pp. 527–581 and references therein.